

Diagnosing Mechanisms of Hydrologic Change under Global Warming in the CESM1 Large Ensemble

NICHOLAS SILER^a, DAVID B. BONAN^b, AND AARON DONOHOE^c

^a College of Earth, Ocean, and Atmospheric Sciences, Oregon State University, Corvallis, Oregon

^b California Institute of Technology, Pasadena, California

^c Polar Science Center/Applied Physics Laboratory, University of Washington, Seattle, Washington

(Manuscript received 16 February 2023, in final form 9 July 2023, accepted 31 August 2023)

ABSTRACT: Global warming is expected to cause significant changes in the pattern of precipitation minus evaporation ($P - E$), which represents the net flux of water from the atmosphere to the surface or, equivalently, the convergence of moisture transport within the atmosphere. In most global climate model simulations, the pattern of $P - E$ change resembles an amplification of the historical pattern—a tendency known as “wet gets wetter, dry gets drier.” However, models also predict significant departures from this approximation that are not well understood. Here, we introduce a new method of decomposing the pattern of $P - E$ change into contributions from various dynamic and thermodynamic mechanisms and use it to investigate the response of $P - E$ to global warming within the CESM1 Large Ensemble. In contrast to previous decompositions of $P - E$ change, ours incorporates changes not only in the monthly means of atmospheric winds and moisture, but also in their temporal variability, allowing us to isolate the hydrologic impacts of changes in the mean circulation, transient eddies, relative humidity, and the spatial and temporal distributions of temperature. In general, we find that changes in the mean circulation primarily control the $P - E$ response in the tropics, while temperature changes dominate at higher latitudes. Although the relative importance of specific mechanisms varies by region, at the global scale departures from the wet-gets-wetter approximation over land are primarily due to changes in the temperature lapse rate, while changes in the mean circulation, relative humidity, and horizontal temperature gradients play a secondary role.

KEYWORDS: Hydrologic cycle; Climate change; Moisture/moisture budget

1. Introduction

The local imbalance between precipitation and evaporation, $P - E$, is among the most important variables in hydrology. Over land, $P - E$ is equal to the combined rates of surface runoff and groundwater storage, and thus sets the upper limit on renewable freshwater resources within a given watershed (Oki and Kanae 2006). Over the ocean, $P - E$ is a leading control on the salinity and stratification of the mixed layer, which plays an important role in the ocean circulation (e.g., de Boyer Montégut et al. 2007), and influences the rate at which the ocean takes up heat and carbon in response to anthropogenic forcing (e.g., Liu et al. 2021). From an atmospheric perspective, $P - E$ equals the net convergence of water vapor transport in the time mean, and thus provides a conceptual framework for understanding how the regional hydrologic cycle will respond to changes in the atmospheric circulation or moisture content. For these reasons, the response of $P - E$ to global warming has been an active area of climate research for decades (e.g., Wetherald and Manabe 2002; Held and Soden 2006).

A natural starting point for thinking about the response of $P - E$ to global warming is the thermodynamic approximation of Held and Soden (2006, hereafter HS06), which is based on

the following line of reasoning. First, if changes in relative humidity are small, the amount of water vapor in the atmosphere will increase almost exponentially with increasing temperature, at a rate of about $7\% \text{ K}^{-1}$ (i.e., the Clausius–Clapeyron scaling factor). Second, if the basic structure and intensity of the atmospheric circulation remains similar under warming, the pattern of atmospheric vapor transport should increase with warming at about the same rate as water vapor. Finally, because $P - E$ is equal to the convergence of vapor transport, it too should amplify at the Clausius–Clapeyron rate, provided that spatial gradients in warming are relatively weak. Such an amplification of the mean-state hydrologic cycle with warming implies that $P - E$ will increase where $P > E$ (“wet gets wetter”) and decrease where $P < E$ (“dry gets drier”).

Although an amplification of mean-state $P - E$ is broadly consistent with the pattern of $P - E$ change predicted by global climate models (GCMs), there are some important differences. At low latitudes, for example, many GCMs predict a contraction of the intertropical convergence zone (ITCZ), where $P - E > 0$, and an expansion of the subtropics, where $P - E < 0$ (Chou and Neelin 2004; Lu et al. 2007; Kang and Lu 2012; Byrne and Schneider 2016; Byrne et al. 2018; Donohoe et al. 2019). At higher latitudes, GCMs tend to predict a poleward shift in the extratropical latitude of maximum $P - E$ associated with the midlatitude storm tracks (e.g., Scheff and Frierson 2012; Siler et al. 2018). None of these changes is consistent with the HS06 paradigm of “wet gets wetter, dry gets drier.” Furthermore, because $P - E$ cannot be negative over land on long time scales, the HS06 approximation cannot explain any decrease in $P - E$ over land,

Supplemental information related to this paper is available at the Journals Online website: <https://doi.org/10.1175/JCLI-D-23-0086.s1>.

Corresponding author: Nicholas Siler, nick.siler@oregonstate.edu

which many GCMs predict will occur in parts of the subtropics and lower midlatitudes (Byrne and O’Gorman 2015).

Why does the pattern of $P - E$ change predicted by GCMs differ from the HS06 approximation? The most obvious reason is that the HS06 approximation does not account for changes in atmospheric dynamics, such as an expansion of the Hadley cells (e.g., Lu et al. 2007), a weakening of the Walker cells (e.g., Power and Kociuba 2011; DiNezio et al. 2013), a shift in stationary eddies (Wills et al. 2016), or changes in the dynamics of extratropical cyclones (O’Gorman and Schneider 2008; Bengtsson et al. 2009). All GCMs predict dynamical changes like these to some degree, and any such change is bound to alter the patterns of vapor transport and thus $P - E$ in ways that are not captured by the HS06 approximation.

But changes in atmospheric dynamics are not the only aspect of climate change that the HS06 approximation leaves out; it also neglects thermodynamic effects associated with changes in the spatial patterns of temperature and relative humidity. More specifically, GCMs generally predict that relative humidity will decrease over land in a warmer climate, and that the magnitude of warming will be amplified over land and at high latitudes. Boos (2012) and Byrne and O’Gorman (2015) both introduced additional terms to the HS06 approximation that account for these changes, and both found that their corrections resulted in better agreement with GCM simulations of $P - E$ change. Similarly, in simulations of global warming performed with a one-dimensional diffusive energy balance model (EBM), Siler et al. (2018) found that the pattern of $P - E$ change more closely resembled that of GCM simulations when warming was amplified at the poles, even though the diffusion coefficient, which represents eddy dynamics within the EBM, was held constant. According to Byrne and O’Gorman (2015), corrections to the HS06 approximation that account for heterogeneous changes in temperature and relative humidity result in a smaller increase in $P - E$ over land, and may explain why, over some land surfaces, $P - E$ is even projected to decrease.

To better understand the thermodynamic and dynamic mechanisms driving the $P - E$ response to global warming in GCM simulations more generally, previous studies have often employed a decomposition method first introduced by Seager et al. (2010), which allows any change in $P - E$ to be separated into contributions from changes in (i) monthly-mean winds (dynamics), (ii) monthly-mean specific humidity (thermodynamics), and (iii) the covariance between winds and specific humidity, which represents vapor transport by transient eddies. This decomposition has provided valuable insight in cases where $P - E$ change is primarily driven by changes in monthly-mean winds or moisture. However, the transient eddy term includes both dynamic and thermodynamic contributions, since it encompasses both changes in eddy dynamics (e.g., storm track shifts) as well as changes in the variance of humidity, which is generally expected to increase due to Clausius–Clapeyron scaling (Byrne and O’Gorman 2015). Thus, the decomposition introduced by Seager et al. (2010) does not permit a full accounting of the dynamic and thermodynamic components of $P - E$ change, nor can it provide insight into the contributions of specific thermodynamic mechanisms, such as

those described by Held and Soden (2006), Boos (2012), Byrne and O’Gorman (2015), and Siler et al. (2018).

In this paper, we introduce a novel decomposition of $P - E$ change that allows us to quantify not only the dynamic and thermodynamic components of the transient-eddy contribution, but also the contributions from various other thermodynamic mechanisms. We explain our approach in section 2 and use it to quantify the total thermodynamic and dynamic components of the $P - E$ response to climate change within the CESM1 Large Ensemble. In section 3, we further decompose the thermodynamic and dynamic components into contributions from monthly-mean and transient-eddy changes, thus providing a first-ever decomposition of the transient-eddy contribution to $P - E$ change. In section 4, we present a new decomposition of the thermodynamic component of $P - E$ change into contributions from specific thermodynamic mechanisms, most of which have been discussed in previous studies. We then use these results in section 5 to reexamine why the HS06 approximation is too wet over land. In section 6, we summarize our results and discuss their implications for other simplified approaches to climate modeling, including the moist energy balance model and the pseudo global warming method of regional climate modeling.

2. A new decomposition of $P - E$ change, applied to the CESM1 Large Ensemble

In this section, we introduce a new method of decomposing the change in annual-mean $P - E$ into thermodynamic and dynamic components and apply it to simulations of global warming from the CESM1 Large Ensemble (CESM1-LE; Kay et al. 2015). The CESM1-LE consists of 40 coupled atmosphere–ocean simulations performed at roughly 1° horizontal resolution over the period 1920–2100. All ensemble members were run with exactly the same model physics and anthropogenic forcing (historical forcing up to 2005 and RCP8.5 afterward), but with slightly perturbed initial conditions in the atmosphere that give each member a unique realization of internal climate variability. Because the amplitude of internal variability decreases when multiple ensemble members are averaged, the response to anthropogenic forcing is well approximated by the change in the ensemble mean (Deser et al. 2012).

We define the response to global warming within the CESM1-LE simulations as the change between two decadal climatologies: one representing the historical climate (1991–2000) and one representing a future warmer climate (2071–80). To conserve computing resources, we limit our analysis to the first 20 ensemble members of the CESM1-LE, for which the ensemble-mean response of surface temperature and $P - E$ is nearly identical to that of the full ensemble (see Fig. 1 in the online supplemental material).

The top row of Fig. 1 shows the pattern of annual-mean $P - E$ in the ensemble mean of the historical climate (Fig. 1a), alongside the change in annual-mean $P - E$ between the historical and warmer climates (Fig. 1b). Results are presented as latent energy fluxes, with 1 W m^{-2} representing approximately 1.3 cm of surface water per year. Figure 1c

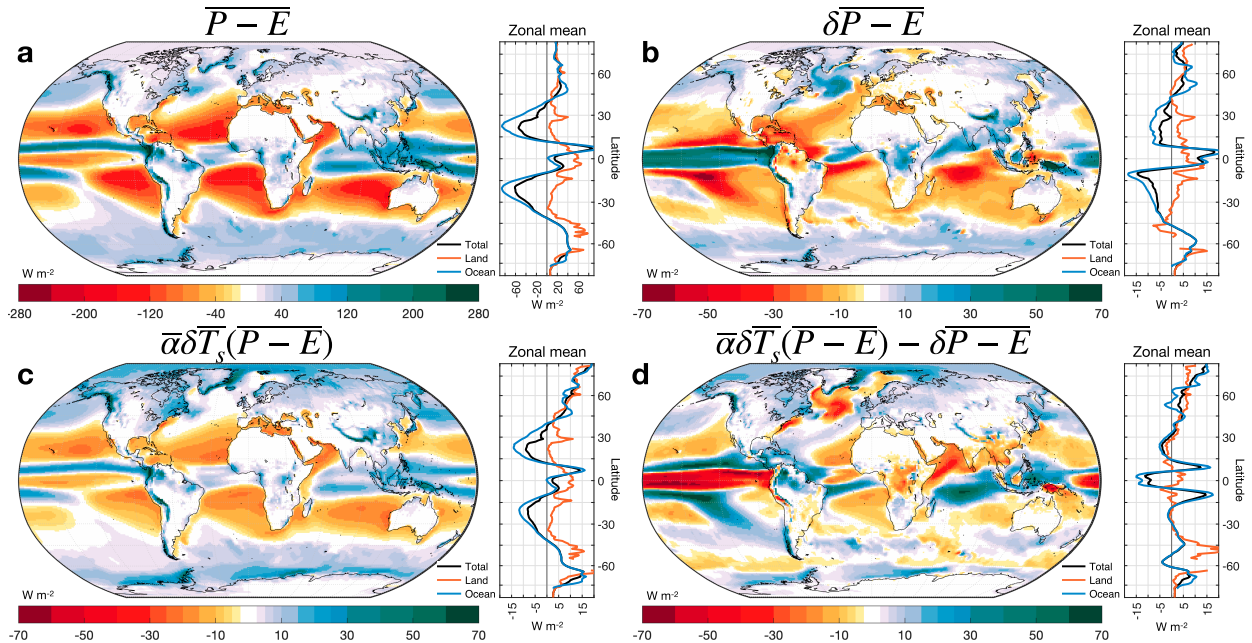


FIG. 1. (a) Annual-mean, ensemble-mean precipitation minus evaporation ($\overline{P - E}$) in the historical climate of the CESM1-LE simulations (1991–2000), expressed as a latent energy flux (in W m^{-2}). (b) The change in $\overline{P - E}$ between the historical climate and the warmer climate (2071–80). (c) An approximation of the change in $\overline{P - E}$ based on Held and Soden (2006), computed with Eq. (1). (d) The difference between the HS06 approximation in (c) and the actual change in $\overline{P - E}$ in (b). Graphs to the right of each map show the zonal mean of each variable over land grid points (red), ocean grid points (blue), and all grid points (black).

shows the HS06 approximation of the change in $P - E$, which we compute as

$$\overline{\delta P - E}_{\text{HS06}} = \overline{\alpha \delta T_s (P - E)}, \quad (1)$$

where

$$\alpha = \frac{L_v}{R_v T_s^2} \quad (2)$$

is the Clausius–Clapeyron scaling factor, T_s is local near-surface air temperature, L_v is the latent heat of vaporization, and R_v is the gas constant for water vapor. Throughout the paper, we use δ to indicate the change between the historical and warmer climates and an overline to indicate the monthly- and ensemble-mean value of a variable in a given location and climate. All results are presented for the annual mean, which we compute as the average of monthly means.

Comparing the true pattern of $\overline{\delta P - E}$ with the HS06 approximation (Figs. 1b,c), we find broad similarities but also important differences, as evidenced by a relatively weak spatial correlation of $r = 0.32$ globally. The difference pattern is shown in Fig. 1d, and is broadly consistent with what other studies have found. In particular, the HS06 approximation tends to exaggerate the magnitude of both the increase in $\overline{P - E}$ over land and at high latitudes and the decrease in $\overline{P - E}$ over subtropical oceans (e.g., Byrne and O’Gorman 2015; Siler et al. 2018). It also does not capture any changes in the spatial pattern of $\overline{P - E}$, which are especially large in the tropics.

We can gain insight into the pattern of $\overline{\delta P - E}$ by analyzing it in terms of the atmospheric moisture budget. From mass conservation, $\overline{P - E}$ must equal the convergence of net atmospheric latent energy transport on long time scales (Trenberth and Guillemot 1995):

$$\overline{P - E} = -\overline{\nabla \cdot \mathbf{F}}, \quad (3)$$

where

$$\mathbf{F} = \frac{L_v}{g} \int_0^{p_s} \mathbf{q} \mathbf{u} dp \quad (4)$$

is a 2D vector representing the column-integrated horizontal latent energy transport, g is the acceleration due to gravity, p_s is surface pressure, q is specific humidity, \mathbf{u} is the horizontal wind vector ($u\mathbf{i} + v\mathbf{j}$), and $(\nabla \cdot)$ is the 2D divergence operator. Likewise, the change in $\overline{P - E}$ under global warming can be expressed as

$$\overline{\delta P - E} = -\frac{L_v}{g} \nabla \cdot \left[\int_0^{p_{s,w}} q_w \mathbf{u}_w dp - \int_0^{p_s} q \mathbf{u} dp \right], \quad (5)$$

where the subscript w indicates the warmer climate and the absence of a subscript indicates the historical climate.

Equation (5) shows that the net change in $\overline{P - E}$ under global warming arises from the product of changes in q (thermodynamics) and changes in \mathbf{u} (dynamics). To better understand the pattern of $\overline{P - E}$ change in Fig. 1b, we seek to quantify the impacts of changes not only in the monthly

means of q and \mathbf{u} , as is commonly done (e.g., Seager et al. 2010), but also of changes in their temporal variability.

We begin our decomposition of $\delta P - \bar{E}$ by isolating the total impact of thermodynamic changes, which we define as any change in the spatial or temporal distribution of q ($\delta q = q_w - q$), assuming no change in \mathbf{u} or p_s :

$$\overline{\delta P - E}_q \approx -\frac{L_v}{g} \nabla \cdot \int_0^{p_s} \delta q \mathbf{u} dp. \quad (6)$$

While this is conceptually similar to the thermodynamic approximation of Seager et al. (2010; see section 3 herein), it is important to emphasize that δq in Eq. (6) does not represent the change in monthly-mean q , as it does in the Seager decomposition, but rather the time-varying change in q that one might expect in a warmer climate given the same dynamical conditions as in the historical climate.

To approximate δq , we first compute the probability density function (PDF) of 6-hourly q for each month, grid point, and pressure level in both the historical and warmer climates. With each climate state simulated by 20 ensemble members, and with a decade of model output from each member, the monthly PDF at each grid point and pressure level comprises about 24 000 data points.¹ Next, we use the historical PDFs to find the percentile rank of q at each location and time step within the historical climate, and estimate δq as the difference between the warmer and historical PDFs at the same percentile. The implicit assumption behind this approach is that the percentile rank of q at a particular time is closely tied to the large-scale circulation, and thus the correlation between q and \mathbf{u} does not change in the percentile sense when \mathbf{u} is held fixed.²

An example of how we use this method to approximate δq is illustrated in Fig. 2, which shows hypothetical PDFs of q for an arbitrary month and location in the historical climate (blue) and the warmer climate (red), with shading representing the extreme tenths of each distribution (i.e., the 10th and 90th percentiles).

Comparing the two PDFs in Fig. 2, we see that the warmer distribution lies to the right of the baseline distribution, indicating a general increase in q under global warming. In addition, the warmer distribution is also broader than the baseline distribution, indicating an increase in the variance of q . Because of this increase in variance, δq will be greater than the change in monthly-mean q ($\delta \bar{q}$) whenever q in the historical simulation is greater than average (i.e., to the right of the blue dashed line). Conversely, δq will be less than $\delta \bar{q}$ whenever q in the historical simulation is less than average (i.e., to the left of the blue dashed line). The opposite relationships would hold if the variance of q were to decrease rather than increase with warming. Changes in the higher-order moments of the q distribution would impact δq in ways that are less

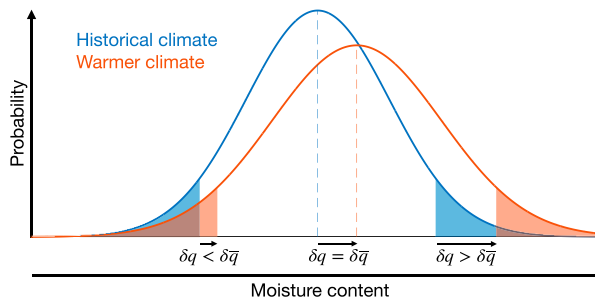


FIG. 2. Schematic probability density functions of atmospheric specific humidity (q) for a particular month and location within the historical climate (blue) and the warmer climate (red). Vertical dashed lines indicate monthly-mean q , while shaded regions indicate the lowest and highest 10% of q values within each distribution. In this hypothetical case, the warmer climate exhibits not only an increase in mean q (i.e., the peak shifts to the right), but also an increase in q variance (i.e., the distribution broadens). As a result, $\delta q < \delta \bar{q}$ when the historical atmosphere is drier than average, while $\delta q > \delta \bar{q}$ when the historical atmosphere is moister than average.

obvious than the simple change in variance depicted in Fig. 2, but those effects are also incorporated with this method.

Next, we seek to approximate the dynamic component of $\overline{\delta P - E}$, which we define as the contribution from changes in \mathbf{u} and p_s ,³ assuming no change in q . This is less straightforward than the thermodynamic approximation because it includes the effects of changes not only in the PDFs of p_s , u , and v , but also in the correlations among them (e.g., Wu et al. 2011). While it might be possible in principle to account for such changes by perturbing p_s and \mathbf{u} in the historical simulation, we do not attempt that here. Instead, we repeat the thermodynamic approximation in Eq. (6), but in reverse: that is, instead of adding a q perturbation at each time step within the historical climate, we subtract a q perturbation at each time step within the warmer climate. This yields an approximation of $\overline{P - E}$ in a hypothetical future climate in which only \mathbf{u} is changed, while the distribution of q is the same as in the historical climate:

$$\overline{P - E}_{\mathbf{u}} \approx -\frac{L_v}{g} \nabla \cdot \int_0^{p_{s,w}} (q_w - \delta q_w) \mathbf{u}_w dp. \quad (7)$$

Here δq_w is identical to δq in Eq. (6), but whereas δq is determined by the percentile rank of q at each time step within the historical climate, δq_w is determined by the percentile rank of q_w at each time step within the warmer climate. Finally, we subtract historical $\overline{P - E}$ from Eq. (7) to get the dynamic component of $\delta \overline{P - E}$:

$$\delta \overline{P - E}_{\mathbf{u}} \approx -\frac{L_v}{g} \nabla \cdot \left[\int_0^{p_{s,w}} (q_w - \delta q_w) \mathbf{u}_w dp - \int_0^{p_s} q \mathbf{u} dp \right]. \quad (8)$$

The top row of Fig. 3 shows the thermodynamic and dynamic contributions to annual-mean $\delta \overline{P - E}$ computed from Eqs. (6) and (8). The sum of these contributions is shown in Fig. 3c; if

³ Because p_s is closely tied to the large-scale circulation, we consider changes in p_s to be part of the dynamic response to warming.

¹ 20 members \times 10 months per member \times \sim 30 days per month \times 4 data points per day = 24 000 data points.

² In reality, changes in the distribution of q may not be entirely thermodynamic, since they may be driven in part by changes in \mathbf{u} (e.g., if storms at a given location became more or less frequent). As we later show, however, the small errors in our decomposition (Fig. 3) suggest that such dynamic influences on the q PDF can generally be neglected.

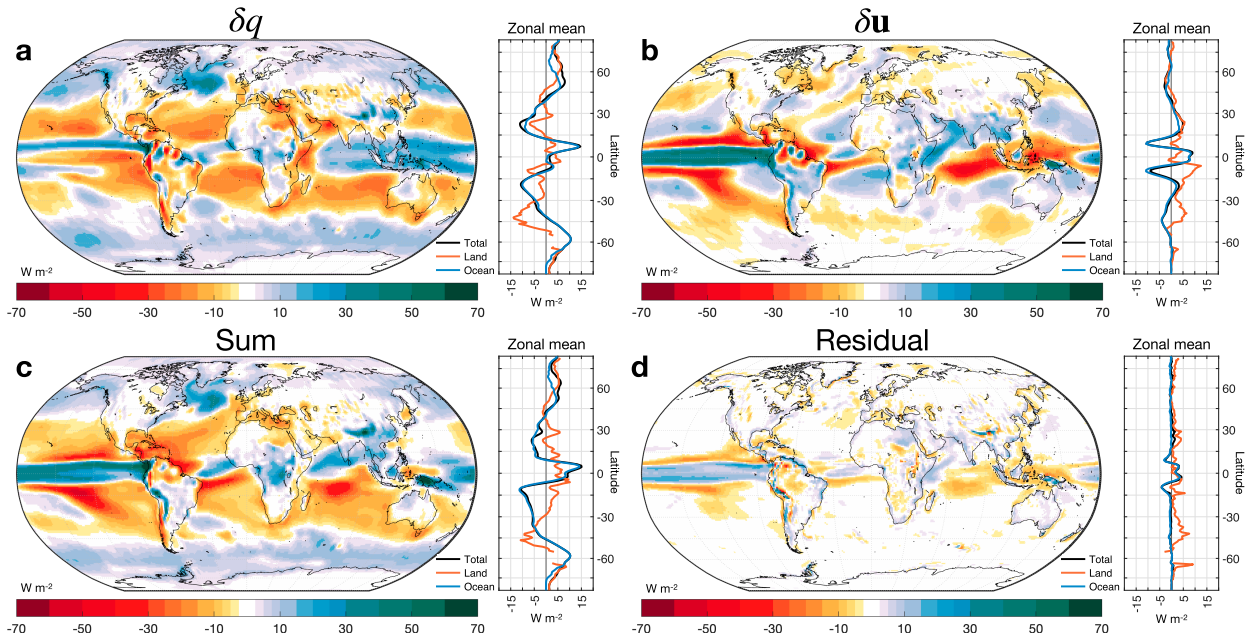


FIG. 3. The contributions to annual-mean $\delta\overline{P} - \overline{E}$ from (a) changes in specific humidity and (b) changes in horizontal winds as defined in Eqs. (6) and (8), respectively. (c) The sum of the thermodynamic and dynamic contributions in (a) and (b). (d) The residual error in the decomposition, representing the difference between the full pattern of $\delta\overline{P} - \overline{E}$ in Fig. 1b and the sum of the individual contributions in (c). Globally, the mean absolute error is 2.9 W m^{-2} , and the spatial correlation between (c) and Fig. 1b is $r = 0.96$.

the decomposition method is accurate, this sum should match the actual pattern of $\delta\overline{P} - \overline{E}$ shown in Fig. 1b. The difference between Figs. 1b and 3c is shown in Fig. 3d and represents the error in the decomposition. Globally, the sum of the thermodynamic and dynamic contributions closely matches the pattern of $\delta\overline{P} - \overline{E}$, with a spatial correlation of $r = 0.96$ and a mean absolute error of 2.9 W m^{-2} .

Some of the error in Fig. 3d is physical, likely stemming from dynamic contributions to changes in the q distribution (see footnote 2 above) or from changes in the percentile correlations between q and the vector wind components (Wu et al. 2011), which our decomposition also neglects. This physical component of the error is found by subtracting Eqs. (6) and (8) from Eq. (5), which simplifies to

$$\delta\overline{P} - \overline{E} - (\delta\overline{P} - \overline{E}_q + \delta\overline{P} - \overline{E}_u) = -\frac{L_v}{g} \nabla \cdot \left[\int_0^{p_{s,w}} \delta q_w \mathbf{u}_w dp \right] - \left[\int_0^{p_s} \delta q u dp \right]. \quad (9)$$

This accounts for about half of the total error in Fig. 3d (supplemental Fig. 2b). The rest can be attributed to our numerical methods (see appendix A). When we compare Fig. 3c to the pattern of $\delta\overline{P} - \overline{E}$ computed from 6-hourly q and \mathbf{u} [Eq. (5); supplemental Fig. 2a], the numerical component of the error is removed and the spatial correlation improves to $r = 0.99$. This shows that, despite its limitations, our decomposition produces highly accurate approximations of the thermodynamic and dynamic contributions to $\delta\overline{P} - \overline{E}$ within the CESM1-LE.

We can evaluate the relative importance of thermodynamic and dynamic changes by comparing the patterns of $\delta\overline{P} - \overline{E}_q$ and $\delta\overline{P} - \overline{E}_u$ in Figs. 3a and 3b against the total pattern of $\delta\overline{P} - \overline{E}$ in Fig. 1b. Globally, $\delta\overline{P} - \overline{E}$ is more strongly correlated with $\delta\overline{P} - \overline{E}_u$ than with $\delta\overline{P} - \overline{E}_q$ ($r = 0.69$ vs 0.31), indicating that dynamic changes are more important than thermodynamic changes to the overall spatial pattern. However, the strength of these correlations varies significantly with latitude. In the deep tropics equatorward of 10°N/S , the pattern of $\delta\overline{P} - \overline{E}$ is nearly identical to $\delta\overline{P} - \overline{E}_u$ ($r = 0.84$), while the correlation with $\delta\overline{P} - \overline{E}_q$ is insignificant ($r = -0.03$). Poleward of 50°N/S , however, we find almost the opposite result, with $\delta\overline{P} - \overline{E}$ far more strongly correlated with $\delta\overline{P} - \overline{E}_q$ than with $\delta\overline{P} - \overline{E}_u$ ($r = 0.78$ vs 0.26). Thus, while the pattern of $\delta\overline{P} - \overline{E}$ is dominated by dynamic changes in the tropics, thermodynamic changes play a greater role at high latitudes, echoing results from previous studies of changes in extreme precipitation (Pfahler et al. 2017; Norris et al. 2019; O’Gorman 2015).

3. Decomposition into monthly-mean and transient components

We can gain further insight into the patterns of $\delta\overline{P} - \overline{E}_q$ and $\delta\overline{P} - \overline{E}_u$ in Fig. 3 by further decomposing them into contributions from monthly-mean and transient changes. Our approach is similar to that of Seager et al. (2010), but with one important difference: in addition to the contributions to $\delta\overline{P} - \overline{E}$ from changes in mean-state dynamics and thermodynamics, we also isolate the dynamic and thermodynamic components of the transient-eddy contribution, which is not possible using the Seager et al. (2010) method.

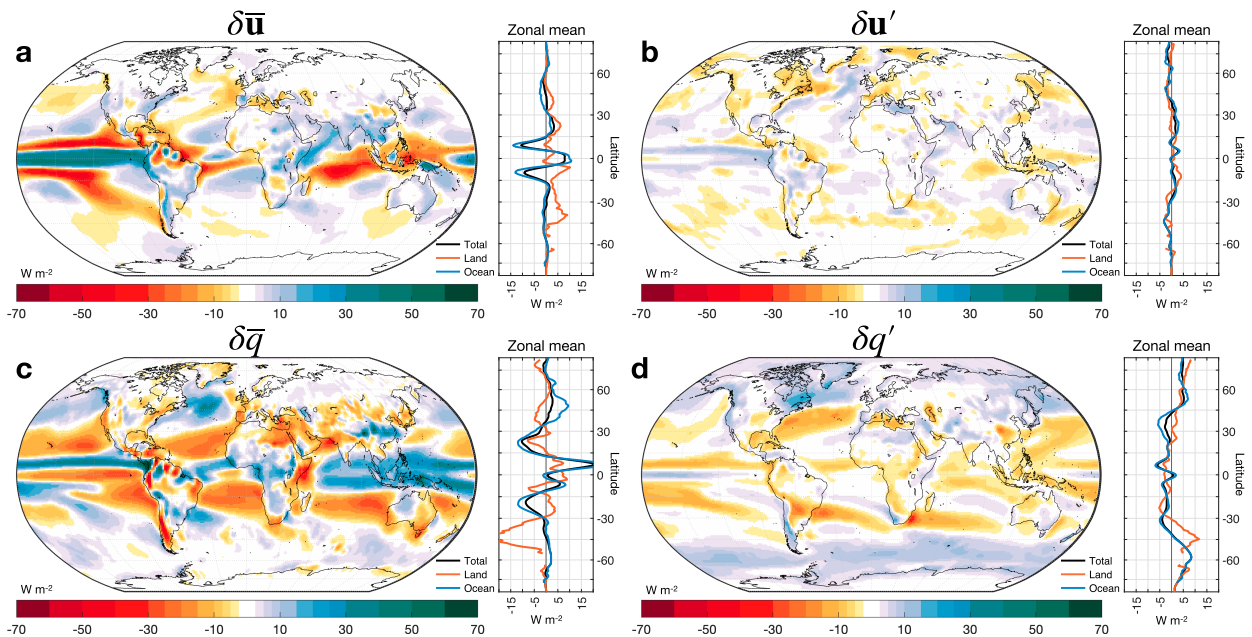


FIG. 4. Contributions to annual-mean $\delta\overline{P - E}$ from changes in (a) monthly-mean dynamics, (b) transient dynamics, (c) monthly-mean specific humidity, and (d) transient specific humidity.

We begin by decomposing q and \mathbf{u} into two components,

$$q = \bar{q} + q', \quad (10)$$

$$\mathbf{u} = \bar{\mathbf{u}} + \mathbf{u}', \quad (11)$$

where overbars represent long-term monthly means and primes represent departures from long-term monthly means (i.e., transients). Because the product of means and transients must equal zero in the time average, Eqs. (3), (4), (10), and (11) combine to give

$$\overline{P - E} = -\frac{L_v}{g} \nabla \cdot \left[\int_0^{p_s} \bar{q} \bar{\mathbf{u}} dp + \int_0^{p_s} q' \mathbf{u}' dp \right], \quad (12)$$

where the first term on the RHS represents the contribution to $\overline{P - E}$ from the monthly-mean circulation and the second (covariance) term represents the contribution from transient eddies.

From Eq. (12), Seager et al. (2010) showed that the response of $\overline{P - E}$ to climate change can be approximated as the sum of four terms:

$$\begin{aligned} \delta(\overline{P - E})_{\text{Seager}} \approx & -\frac{L_v}{g} \int_0^{p_s} \nabla \cdot [\delta\bar{q} \bar{\mathbf{u}} + \bar{q} \delta\bar{\mathbf{u}} + \delta(q' \mathbf{u}')] dp \\ & - \frac{L_v}{g} \delta(q_s \mathbf{u}_s \nabla p_s). \end{aligned} \quad (13)$$

The first two terms on the RHS of Eq. (13) have a clear physical meaning, representing the impact of changes in monthly-mean thermodynamics ($\delta\bar{q}$) and monthly-mean dynamics ($\delta\bar{\mathbf{u}}$). In contrast, the two remaining terms, which represent the impact of changes in transient-eddy transport and surface vapor convergence, encompass both thermodynamic and dynamic elements,

and are thus harder to interpret. The ambiguity of the eddy term, in particular, makes it impossible to separate the impacts of dynamic changes in the storm tracks ($\delta\mathbf{u}'$) from thermodynamic changes in the variance of q ($\delta q'$).

In our decomposition, by contrast, $\delta\overline{P - E}_q$ and $\delta\overline{P - E}_u$ include the impacts of changes not only in the monthly means of q and \mathbf{u} , but also in their temporal distributions. Because of this, we can compute the mean-state terms in the conventional way,

$$\delta\overline{P - E}_q = -\frac{L_v}{g} \nabla \cdot \int_0^{p_s} \delta\bar{q} \bar{\mathbf{u}} dp, \quad (14)$$

$$\delta\overline{P - E}_u = -\frac{L_v}{g} \nabla \cdot \int_0^{p_s + \delta p_s} \bar{q} \delta\bar{\mathbf{u}} dp, \quad (15)$$

and then solve for the transient terms as residuals⁴:

$$\delta\overline{P - E}_{q'} \approx \delta\overline{P - E}_q - \delta\overline{P - E}_q, \quad (16)$$

$$\delta\overline{P - E}_{u'} \approx \delta\overline{P - E}_u - \delta\overline{P - E}_u. \quad (17)$$

This four-part decomposition of annual-mean $\delta\overline{P - E}$ is shown in Fig. 4. The dynamic components in the top row

⁴ As evident from Eq. (15), the $\delta\bar{\mathbf{u}}$ term formally includes the effects of changes in monthly-mean surface pressure (δp_s), though accounting for this change has no discernible effect on the result (not shown). Similarly, the $\delta\mathbf{u}'$ term includes the effects of changes in transient surface pressure, but these are likely much weaker than the effects of changes in transient winds. Meanwhile, the surface-pressure term in Eq. (13) does not appear in our decomposition because the divergence operator in Eqs. (14) and (15) remains outside the vertical integrals.

represent the contributions from changes in monthly-mean winds ($\delta\bar{\mathbf{u}}$; Fig. 4a) and transient winds ($\delta\mathbf{u}'$; Fig. 4b). Globally, the monthly-mean component is far more important than the transient component (Fig. 4a vs Fig. 4b). It accounts for nearly all of $\delta\bar{P} - \bar{E}_u$ in the tropics, where $\bar{P} - \bar{E}$ is strongly influenced by the Hadley, Walker, and monsoonal circulations, and it also has a significant impact in parts of the midlatitudes, likely due to changes in stationary eddies (Wills et al. 2016).

Compared with the monthly-mean component, the transient component of the dynamic contribution ($\delta\bar{P} - \bar{E}_w$) is much weaker globally, but it has a greater impact in much of the middle and high latitudes where $\bar{P} - \bar{E}$ is largely driven by transient eddies (Fig. 4b). It tends to be positive in the tropics and negative at higher latitudes, indicating a reduction in poleward latent-heat transport due to changes in eddy dynamics (supplemental Fig. 3). This result is somewhat surprising, since previous studies have found that eddy activity will shift poleward and perhaps even intensify under global warming, especially in the Southern Hemisphere (O’Gorman 2010). However, while the CESM1-LE simulations do exhibit such a poleward shift within the upper troposphere, where eddy activity is strongest, they exhibit a widespread decrease in eddy activity within the lower troposphere, where vapor transport is concentrated (supplemental Fig. 4). Over land, such changes in eddy dynamics contribute to a significant decrease in $\bar{P} - \bar{E}$ over the western United States, western Europe, and eastern Canada, and an increase in $\bar{P} - \bar{E}$ over tropical South America. We discuss the implications of this result for regional climate prediction in section 6.

Next, we consider the thermodynamic components of $\delta\bar{P} - \bar{E}$ shown in the bottom row of Fig. 4. Like the dynamic components, the monthly-mean thermodynamic component ($\delta\bar{q}$; Fig. 4c) is stronger than the transient component at low latitudes while the transient component ($\delta q'$; Fig. 4d) is stronger outside the tropics. To first order, these terms resemble an amplification of the monthly-mean and transient components of $\bar{P} - \bar{E}$ within the historical climate [i.e., the two terms on the RHS of Eq. (12); supplemental Fig. 5]. This result is consistent with the HS06 approximation, which makes no distinction between $\bar{P} - \bar{E}$ from the mean circulation and $\bar{P} - \bar{E}$ from transient eddies [Eq. (1)]. The reason is that, given fixed dynamics and constant relative humidity, all percentiles of the q distribution will scale with warming at about the same rate ($\alpha \approx 7\% \text{ K}^{-1}$), resulting in a similar amplification of both \bar{q} and q' in Eq. (12) (Norris et al. 2019). Beyond this first-order validation of the HS06 approximation, however, the decomposition of $\delta\bar{P} - \bar{E}_q$ into monthly-mean and transient components provides little insight into the underlying thermodynamic mechanisms. For that we turn to a different decomposition of $\delta\bar{P} - \bar{E}_q$, which we derive below.

4. Thermodynamic mechanisms

As noted previously, the HS06 approximation is not identical to $\delta\bar{P} - \bar{E}_q$ because it neglects changes in relative humidity and variability (both spatial and temporal) in the magnitude of warming (Boos 2012; Byrne and O’Gorman 2015; Siler et al. 2018). In this section, we introduce a new decomposition of $\delta\bar{P} - \bar{E}_q$ that allows the contributions from these additional thermodynamic changes to be quantified.

We begin by decomposing $\delta\bar{P} - \bar{E}_q$ into two components: one due to changes in temperature T and the other due to changes in relative humidity H :

$$\delta\bar{P} - \bar{E}_q = \delta\bar{P} - \bar{E}_T + \delta\bar{P} - \bar{E}_H. \quad (18)$$

To find $\delta\bar{P} - \bar{E}_T$, we assume that H is fixed and approximate the thermodynamic change in q from the Clausius–Clapeyron equation:

$$\delta q_T \approx q(e^{\alpha\delta T} - 1), \quad (19)$$

where α is the Clausius–Clapeyron scaling factor [Eq. (2)] and δT is the temperature change between the historical and warmer climates, assuming no change in dynamics. We estimate δT in the same way that we estimated δq in section 2: by computing the PDFs of T in both the historical and warmer climates, and assuming that the percentile of T always remains the same under fixed dynamics (see Fig. 2). Substituting δq_T into Eq. (6) gives

$$\delta\bar{P} - \bar{E}_T \approx -\frac{L_v}{g} \nabla \cdot \int_0^{p_s} \delta q_T \mathbf{u} dp. \quad (20)$$

Subtracting $\delta\bar{P} - \bar{E}_T$ from $\delta\bar{P} - \bar{E}_q$ [Eq. (6)] then yields the contribution from δH :

$$\delta\bar{P} - \bar{E}_H \approx -\frac{L_v}{g} \nabla \cdot \int_0^{p_s} (\delta q - \delta q_T) \mathbf{u} dp. \quad (21)$$

We discuss the impact of changes in relative humidity later in this section, but first we focus on the mechanisms governing the temperature contribution [Eq. (20)]. If δT were uniform in space and time, Eq. (20) would give a result very similar to the HS06 approximation [Eq. (1)]. As previous studies have shown, however, spatial and temporal variability in δT can impact $\delta\bar{P} - \bar{E}_T$ in important ways that are not captured by the HS06 approximation (Boos 2012; Byrne and O’Gorman 2015; Siler et al. 2018; Bonan et al. 2023).

To quantify these impacts, we first decompose δT into monthly-mean and transient components:

$$\delta T = \delta\bar{T} + \delta T'. \quad (22)$$

Combined with Eq. (19), this yields

$$\delta q_T = q(e^{\alpha\delta\bar{T}} e^{\alpha\delta T'} - 1). \quad (23)$$

Because $\alpha\delta T' \ll 1$ everywhere (supplemental Fig. 6), we can replace $e^{\alpha\delta T'}$ in Eq. (23) with its first-order Taylor approximation, $1 + \alpha\delta T'$. This yields

$$\delta q_T \approx q(\beta\delta\bar{T} + \alpha\delta T'[1 + \beta\delta\bar{T}]), \quad (24)$$

where

$$\beta \equiv \frac{e^{\alpha\delta\bar{T}} - 1}{\delta\bar{T}} \quad (25)$$

is a modified Clausius–Clapeyron scaling factor, representing the fractional change in q per degree of monthly-mean

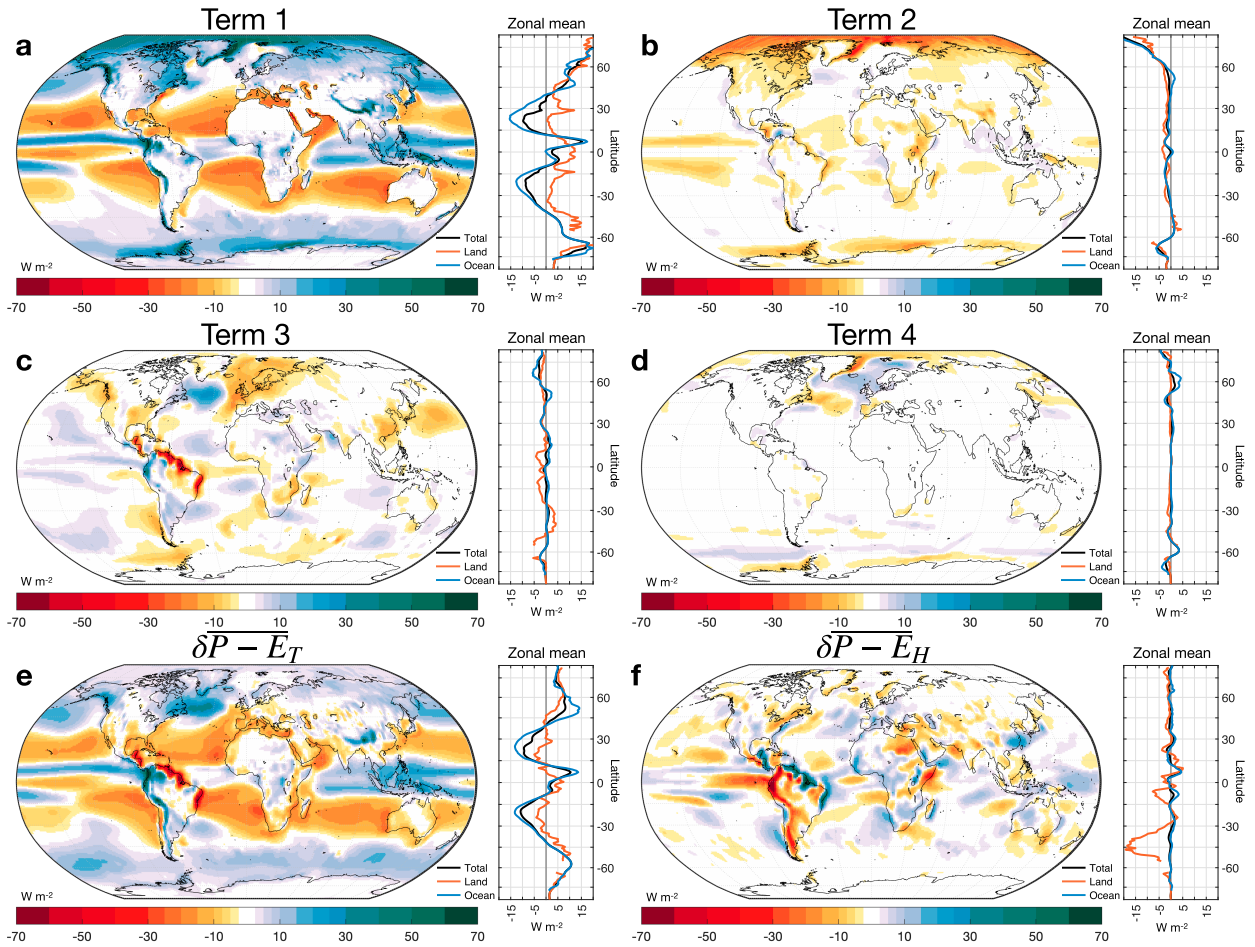


FIG. 5. (a)–(d) The four terms on the RHS of Eq. (28). (e) Annual-mean $\overline{\delta P - E_T}$, which is equal to the sum of the four terms in (a)–(d) and represents the total impact of temperature changes. (f) Annual-mean $\overline{\delta P - E_H}$, which represents the impact of changes in relative humidity.

warming, assuming no change in the shape of the temperature distribution (i.e., $\delta T' = 0$). From the Taylor expansion of β about $\delta \bar{T} = 0$,

$$\beta \approx \alpha \left[1 + \frac{\alpha \delta \bar{T}}{2} + \frac{(\alpha \delta \bar{T})^2}{6} + \dots \right], \quad (26)$$

we can see that the difference between β and α is negligible where $\alpha \delta \bar{T} \ll 1$, but grows larger as $\delta \bar{T}$ increases. The second-order term is comparable in magnitude when $\alpha \delta \bar{T} \approx 2$, which corresponds to about 30 K of warming given $\alpha \approx 7\% \text{ K}^{-1}$.

Finally, to assess the impact of variations in $\delta \bar{T}$ with altitude, we express $\beta \delta \bar{T}$ as

$$\beta \delta \bar{T} = \beta_s \delta \bar{T}_s + (\beta \delta \bar{T} - \beta_s \delta \bar{T}_s), \quad (27)$$

where the s subscript indicates the near-surface atmosphere. The first term on the RHS of Eq. (27) represents the fractional change in q at the surface due to monthly-mean warming, while the term in parentheses represents the departure

from this scaling above the surface due to changes in the monthly-mean lapse rate ($d\bar{T}/dp$).

Combining Eqs. (20), (24), and (27), we can express $\overline{\delta P - E_T}$ as the sum of four terms (see appendix B):

$$\begin{aligned} \overline{\delta P - E_T} \approx & \underbrace{\beta_s \delta \bar{T}_s (\overline{P - E})}_{\text{Term 1}} - \underbrace{\frac{L_v}{g} \int_0^{p_s} (\beta \delta \bar{T} - \beta_s \delta \bar{T}_s) \nabla \cdot (q\mathbf{u}) dp}_{\text{Term 2}} \\ & - \underbrace{\frac{L_v}{g} \int_0^{p_s} \nabla (\beta \delta \bar{T}) \cdot (q\mathbf{u}) dp}_{\text{Term 3}} \\ & - \underbrace{\frac{L_v}{g} \nabla \cdot \int_0^{p_s} \alpha \delta T' (1 + \beta \delta \bar{T}) q \mathbf{u} dp}_{\text{Term 4}}. \end{aligned} \quad (28)$$

The top two rows of Fig. 5 show the annual-mean contributions of each term in Eq. (28), while the bottom row shows the total contributions from changes in temperature and relative humidity ($\overline{\delta P - E_T}$ and $\overline{\delta P - E_H}$). We discuss the contribution of each term and its physical significance below.

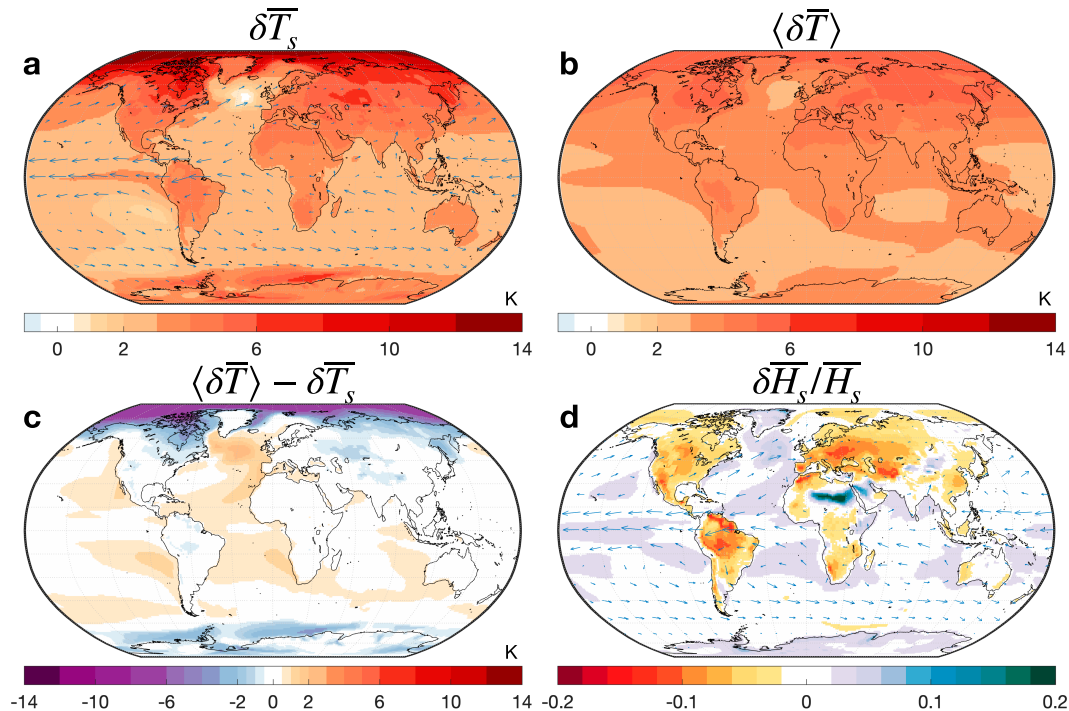


FIG. 6. (a) Annual-mean, ensemble-mean change in near-surface air temperature between the decades 1991–2000 and 2071–80. Blue arrows indicate the direction and relative magnitude of \mathbf{F} in the annual/ensemble mean from 1991 to 2000. (b) The q -weighted column average of temperature change between the decades 1991–2000 and 2071–80 [Eq. (29)]. (c) The difference between (a) and (b), with red colors indicating more warming at the surface than in the column mean (i.e., an increase in the lower-tropospheric lapse rate). (d) As in (a), but for the fractional change in near-surface relative humidity.

a. Term 1: The HS06 approximation

The first term in the decomposition (Fig. 5a) is a slightly modified version of the HS06 approximation [Eq. (1)] and represents the Clausius–Clapeyron amplification of $\overline{P - E}$ in response to surface warming. Like the original HS06 approximation, it has the same spatial structure as $\overline{P - E}$ (Fig. 1a), but with relatively greater magnitudes at high latitudes where δT_s and β are both amplified (Fig. 6a). Among the four terms in Eq. (28), it is the most important, as indicated by its strong correlation with the full pattern of $\delta \overline{P - E}_T$ globally (Fig. 5e; $r = 0.78$). However, there are some regions—especially over land, in the North Atlantic, and at high latitudes—where it differs significantly from $\delta \overline{P - E}_T$. It is also too moist globally, averaging 7 W m^{-2} when in reality, mass conservation requires that $\delta \overline{P - E} = 0$ in the global mean.

b. Term 2: Change in the monthly-mean lapse rate

The second term in Eq. (28) is shown in Fig. 5b. It has the largest impact at high latitudes, where it offsets most of the increase in $\overline{P - E}$ predicted by the HS06 approximation (term 1). The reason for this can be inferred from Fig. 6, which shows the pattern of δT_s (Fig. 6a) alongside the q -weighted column-mean temperature change $\langle \delta T \rangle$, which represents the mean warming experienced by *all* vapor in the atmospheric column (Fig. 6b):

$$\langle \delta T \rangle = \frac{\int_0^{p_s} \delta T q dp}{\int_0^{p_s} q dp}. \quad (29)$$

The difference between Figs. 6a and 6b is shown in Fig. 6c and is a rough indicator of the change in the lower-tropospheric lapse rate. If warming were uniform in height, the lapse rate would not change and term 2 would vanish. At high latitudes, however, the loss of snow and sea ice enhances solar heating of the surface (e.g., Feldl et al. 2020), causing a large increase in the lower-tropospheric lapse rate ($\delta T_s - \langle \delta T \rangle > 0$; Fig. 6c). By assuming that $\overline{P - E}$ scales with surface warming, the HS06 approximation neglects this effect, and thus overestimates the increase in $\overline{P - E}$ at high latitudes (Fig. 5a). Term 2 corrects for this, explaining its strong negative contribution to $\delta \overline{P - E}$ at high latitudes.

At lower latitudes, by contrast, the difference between δT_s and $\langle \delta T \rangle$ is relatively small (Fig. 6c). This may seem surprising given that the lapse rate robustly decreases at these latitudes, but in reality, the magnitude of the lapse-rate change is significantly smaller at low latitudes than at high latitudes, especially within the lower troposphere where vapor is concentrated (Feldl et al. 2020; Taylor et al. 2022). This does not explain why term 2 is robustly negative at low latitudes—indeed, it is

perplexing that this result holds regardless of whether $\overline{P - E}$ is positive or negative—but it does explain why the magnitude of term 2 is generally small at these latitudes.

c. Term 3: Horizontal warming gradients

The third term in Eq. (28) is shown in Fig. 5c. Physically, this term represents the contribution to $\delta\overline{P - E}$ from horizontal gradients in $\beta\delta\overline{T}$. If we ignore the (small) gradients in β and assume no change in the lapse rate, term 3 simplifies to

$$\text{Term 3} \approx -\beta\nabla(\delta\overline{T}_s) \cdot \overline{\mathbf{F}}, \quad (30)$$

which is nearly identical to the correction that Boos (2012) introduced to the HS06 approximation to account for gradients in $\delta\overline{T}_s$ during the Last Glacial Maximum.

The impact of warming gradients is evident in Fig. 6a, which shows annual-mean \mathbf{F} in blue arrows overlaying $\delta\overline{T}_s$. Comparing this figure to the pattern of $\delta\overline{P - E}$ in Fig. 5c, we find that term 3 contributes to an increase in vapor divergence—and thus a decrease in $\delta\overline{P - E}$ —in regions where warming is amplified downstream (i.e., in the direction of vapor transport). This applies to much of the extratropics, where $\overline{\mathbf{F}}$ is generally poleward and warming tends to increase with latitude. It is also true along the eastern coast of tropical South America, where amplified warming over land results in weaker convergence of vapor transport from the Atlantic. Conversely, we find an increase in $\overline{P - E}$ in regions where the magnitude of warming weakens downstream, such as along the western coast of South America and in the subpolar North Atlantic, where warming is suppressed due to changes in ocean circulation (Marshall et al. 2015; Menary and Wood 2018). This contradicts the hypothesis that the increase in $\overline{P - E}$ over the North Atlantic warming hole is driven by changes in storm dynamics resulting from locally enhanced baroclinicity (Smith et al. 2021).

d. Term 4: Change in temperature variance

Figure 5d shows the contribution from the fourth term in Eq. (28). This term captures the impact on $\overline{P - E}$ from $\delta T'$, which results from a change in the shape of the temperature distribution. It is generally weaker than the other terms, with significant contributions in parts of the North Atlantic and Southern Ocean, but essentially no contribution at low latitudes or over land.

We can gain insight into the physical meaning of the $\delta T'$ contribution by making two simplifying approximations. First, we ignore the factor of $1 + \beta\delta\overline{T}$ inside the integral, since this is close to 1 at all but the highest latitudes and has little impact on the overall spatial pattern. Second, we assume that vertical variations in $\alpha\delta T'$ are small, which allows it to be brought outside the integral. Given these approximations, term 4 simplifies to

$$\text{Term 4} \approx -\nabla \cdot \overline{\alpha\delta T' \mathbf{F}'}, \quad (31)$$

where only the transient component of \mathbf{F} contributes because $\overline{\alpha\delta T' \mathbf{F}} \approx 0$. Equation (31) implies that $\delta T'$ only contributes to $\delta\overline{P - E}$ if the magnitude of warming is correlated with the direction of vapor transport.

To understand why such a correlation might exist, consider that in the middle and high latitudes vapor is primarily transported by eddies mixing across large-scale gradients in \overline{T} and \overline{q} , with moist air flowing downgradient within the storm's warm sector and drier air flowing upgradient within the cold sector. If $\nabla\overline{T}$ weakens under warming (due, for example, to polar amplification), the moist air in the warm sector will experience less warming than the dry air in the cold sector, resulting in a decrease in temperature variance (e.g., Screen 2014; see supplemental Fig. 6) and a smaller increase in *net* \mathbf{F} than would be expected from Clausius–Clapeyron scaling alone. Understood in this way, term 4 has much the same physical meaning as other corrections to the HS06 approximation that have been derived from mixing-length theory, in which the eddy component of \mathbf{F} is assumed to be proportional to $-\nabla\overline{q}$ (Byrne and O’Gorman 2015; Siler et al. 2018). In both frameworks, a weaker temperature gradient offsets some of the increase in $\nabla\overline{q}$ due to Clausius–Clapeyron scaling, thus causing \mathbf{F} to increase with warming at a lower rate than \overline{q} itself.

e. Change in relative humidity

Finally, Fig. 5f shows $\delta\overline{P - E}_H$, which represents the impact of changes in relative humidity [Eq. (21)]. Globally, the magnitude of this term is small compared to that of $\delta\overline{P - E}_T$ (Fig. 5e), implying that most of the change in q under global warming is due to Clausius–Clapeyron scaling, not to changes in H . Moreover, much of the spatial pattern of $\delta\overline{P - E}_H$ seems to be closely tied to Fig. 5c, which represents the impact of horizontal warming gradients [term 3 in Eq. (28)]. Indeed, over tropical land surfaces⁵ where $\delta\overline{P - E}_H$ has the largest impact, Figs. 5c and 5f largely offset each other, with a spatial correlation of $r = -0.78$.

The reason for this cancellation is evident in Fig. 6d, which shows the fractional change in near-surface H along with vectors representing annual-mean \mathbf{F} (as in Fig. 6a). Comparing Figs. 6a and 6d, we see that, with the exception of high latitudes, amplified warming over land generally coincides with a decrease in H , thus offsetting some of the increase in q that would result from Clausius–Clapeyron scaling alone. According to Byrne and O’Gorman (2018), this effect can be explained by two constraints: (i) moist static energy increases by about the same amount over land and ocean at low latitudes and (ii) surface moisture is limited over land, causing a smaller increase in latent energy (q) and a larger increase in enthalpy (T). This highlights an important caveat to our results: even though $\delta\overline{P - E}$ can be mathematically separated into components representing distinct physical mechanisms, we should not assume that these mechanisms are always physically independent.

5. Contributions to $\delta\overline{P - E}$ over land

In the preceding two sections, we decomposed the pattern of $\delta\overline{P - E}$ into seven terms, representing the impact of

⁵ All land equatorward of 30° latitude in both hemispheres.

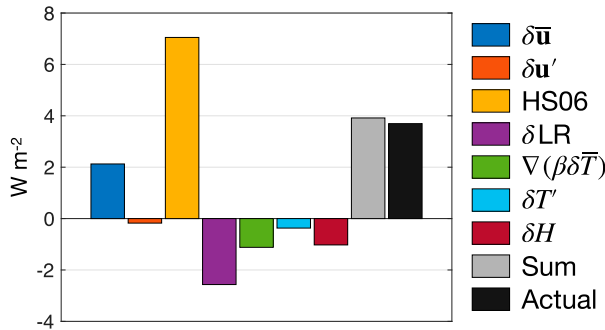


FIG. 7. The annual-mean, global-mean contribution to $\delta\overline{P-E}$ over land from changes in monthly-mean dynamics ($\delta\bar{u}$; blue), changes in transient dynamics ($\delta u'$; red), the HS06 approximation (yellow), changes in the mean lapse rate (δLR ; purple), changes in horizontal temperature gradients ($\nabla[\beta\delta\bar{T}]$; green), changes in temperature variance ($\delta T'$; cyan), and changes in relative humidity (δH ; maroon). The sum of all terms is shown in gray, and the actual change in $\overline{P-E}$ over land is shown in black.

changes in monthly-mean dynamics, transient dynamics, relative humidity, and four aspects of the spatial and temporal distribution of temperature. In light of these results, we now revisit the question that motivated much of the Byrne and O’Gorman (2015) analysis: namely, why does $\overline{P-E}$ over land increase by a smaller amount in climate model simulations than predicted by the HS06 approximation?

To answer this question, we plot in Fig. 7 the average global land contribution to $\delta\overline{P-E}$ from each of the seven different terms. Our results echo those of Byrne and O’Gorman (2015) in important ways. In particular, like Byrne and O’Gorman,

we find that the HS06 approximation exaggerates the increase in $\overline{P-E}$ over land (Fig. 7, yellow bar), and that warming gradients and changes in relative humidity—while partially cancelling each other at regional scales—both contribute to a decrease in $\overline{P-E}$ over land at global scales, offsetting some of the amplification of $\overline{P-E}$ predicted by the HS06 approximation (Fig. 7, green and maroon bars).

But Fig. 7 also highlights some limitations of the Byrne and O’Gorman (2015) analysis, at least in the context of the CESM1-LE simulations. For example, whereas Byrne and O’Gorman emphasized the role of eddies mixing across an altered temperature gradient, we find that this mechanism—represented in our decomposition by a change in temperature variance $\delta T'$ —has little impact on $\overline{P-E}$ over land. Conversely, Byrne and O’Gorman did not consider the role of lapse-rate changes, which our analysis identifies as the primary reason why the HS06 approximation is too wet over land in the global mean (Fig. 7, purple bar).

At regional scales, the relative importance of each mechanism can differ substantially from the global-mean picture presented in Fig. 7. This is evident in Fig. 8, which shows the same breakdown of $\delta\overline{P-E}$ as in Fig. 7, but for five different regions representing a diverse range of hydroclimates (outlined in green). In the western United States and western Europe, for example, changes in eddy dynamics cause a decrease in $\overline{P-E}$ of 32% and 23% relative to the historical average, despite having almost no effect over land in the global mean (Fig. 7). It is also interesting to compare the tropical regions of Africa and South America, which exhibit changes in $\overline{P-E}$ of opposite sign. From Fig. 8, this difference can be attributed to three terms: the change in monthly-mean dynamics, which has little effect in South America but contributes to substantial moistening in Africa, and changes in relative

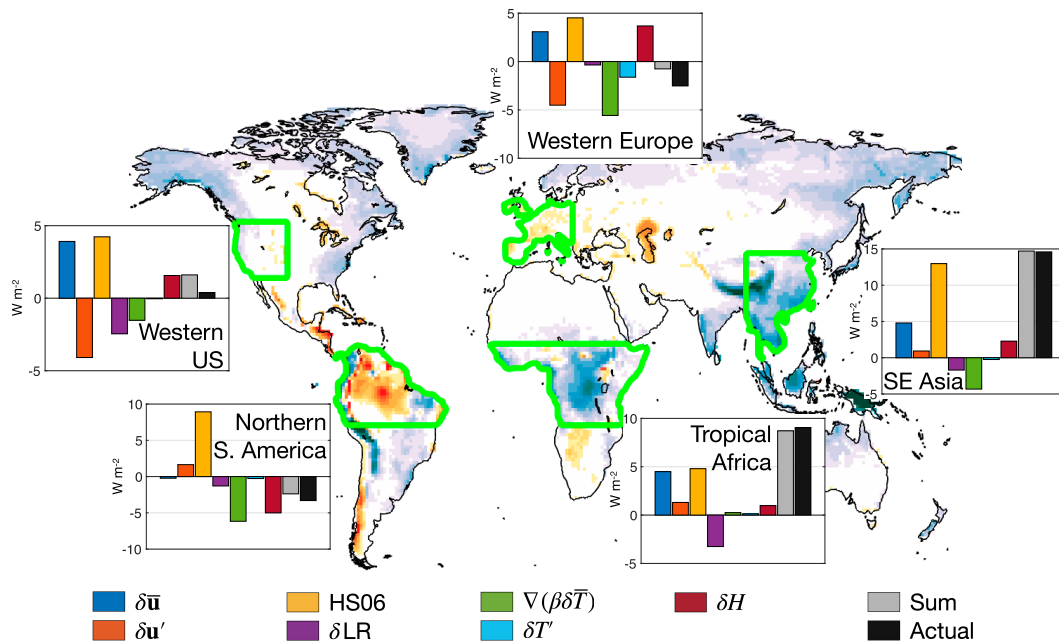


FIG. 8. Annual-mean $\delta\overline{P-E}$ over land (map), using the same color bar shown in Fig. 1b. Inset bar graphs are as in Fig. 7, but for specific regions outlined in green.

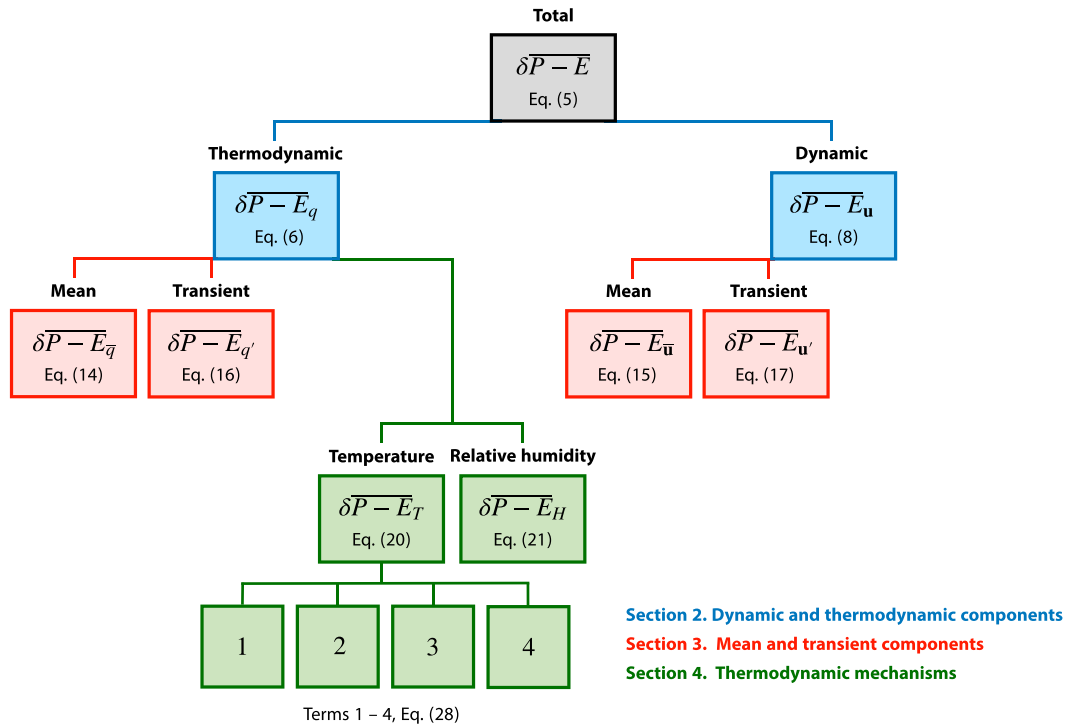
Decomposition of $P - E$ change

FIG. 9. A summary of the various decompositions of $\delta\overline{P - E}$ and their corresponding equations presented in sections 2–4. Blue boxes represent the total contributions from changes in thermodynamics and dynamics (section 2). Red boxes represent the monthly-mean and transient components of the thermodynamic and dynamic contributions (section 3). Green boxes represent a different decomposition of the thermodynamic term, first into contributions from changes in temperature and relative humidity, and then a further decomposition of the temperature contribution into four different terms (section 4). The red boxes can be interpreted as an extension of the Seager et al. (2010) decomposition, while the green boxes address thermodynamic mechanisms discussed by Held and Soden (2006), Boos (2012), Byrne and O’Gorman (2015), and Siler et al. (2018).

humidity and horizontal temperature gradients, which have little effect in Africa but contribute to substantial drying in South America. Meanwhile, in Southeast Asia, the HS06 approximation is fairly accurate, but only because the moistening effects of circulation changes and the drying effects of horizontal warming gradients almost exactly offset each other. These examples highlight the diverse range of hydrologic changes that can occur at regional scales, and the ability of our method to shed light on their underlying causes.

6. Summary and discussion

In this paper, we have introduced a new method of decomposing the response of $P - E$ to climate change into thermodynamic and dynamic components and have used it to better understand the mechanisms governing the change in annual-mean $P - E$ ($\delta\overline{P - E}$) simulated by the CESM1 Large Ensemble. A summary of our approach and key equations is given in Fig. 9. In section 2, we decompose $\delta\overline{P - E}$ into contributions from the total changes in thermodynamics ($\delta\overline{P - E}_q$) and dynamics ($\delta\overline{P - E}_u$) (Fig. 9, blue boxes). In section 3, we decompose both of these terms into

monthly-mean and transient components (Fig. 9, red boxes). The monthly-mean components are similar to terms in the Seager et al. (2010) decomposition, while the transient components represent the first-ever decomposition of the transient-eddy contribution to $\delta\overline{P - E}$, which Seager et al. (2010) treat as a single term. To first order, both the monthly-mean and transient components of $\delta\overline{P - E}_q$ resemble an amplification of the monthly-mean and transient components of historical $P - E$, as predicted by the HS06 approximation. To quantify the influence of additional thermodynamic mechanisms, we further decompose $\delta\overline{P - E}_q$ into contributions from changes in relative humidity ($\delta\overline{P - E}_H$), as well as four terms representing different aspects of temperature change (Fig. 9, green boxes).

Some of our key findings are as follows:

- Dynamic changes explain most of the pattern of annual-mean $\delta\overline{P - E}$ in the tropics, while thermodynamic changes play a dominant role at higher latitudes.
- Changes in transient-eddy dynamics tend to cause $\overline{P - E}$ to increase at low latitudes and decrease at middle and high latitudes, consistent with a reduction in poleward latent-heat transport due to weakened eddy activity. This effect is generally

small, but of first-order importance in some regions, including the western United States and western Europe.

- Lapse-rate changes act to offset much of the increase in $P - E$ predicted by the HS06 approximation at high latitudes, and are the primary reason why the HS06 approximation is too wet over land globally.
- Other departures from the HS06 approximation over land can be attributed to changes in relative humidity (δH) and to horizontal gradients in warming ($\nabla \delta T$). The effects of these changes largely offset each other at regional scales, but both act to decrease $\overline{P - E}$ over land at global scales.

Our results clarify the strengths and weaknesses of two simplified approaches to climate modeling. First, in the moist energy balance model (EBM) of Siler et al. (2018), tropical $\overline{P - E}$ can be altered by changes in the Hadley circulation, but the change in extratropical $\overline{P - E}$ is essentially thermodynamic, resulting from eddies mixing across altered gradients of T and q . This behavior is broadly validated by our results here, which show that the thermodynamic component of $\delta \overline{P - E}$ is dominant in the extratropics while the dynamic component is primarily associated with changes in the tropical mean circulation (Figs. 4a,b). This helps explain why the EBM is able to capture much of the variability in zonal-mean $\delta \overline{T}$ and $\delta \overline{P - E}$ across different GCMs based only on their unique patterns of radiative forcing, feedbacks, and ocean heat uptake (Siler et al. 2018; Bonan et al. 2023).

Second, many recent analyses of the regional impacts of climate change have been based on high-resolution “pseudo global warming” (PGW) simulations, in which historical boundary conditions are perturbed with monthly-mean changes in winds, temperature, relative humidity, and geopotential height diagnosed from GCM simulations. Among the mechanisms identified in this paper, the PGW method omits only the contributions from changes in transient dynamics ($\delta \mathbf{u}'$; Fig. 4b) and transient temperature (δT ; Fig. 6d). Both of these terms tend to be small, suggesting that the PGW method should in general be quite accurate. However, there are some regions, such as the western United States and western Europe, where the contribution from $\delta \mathbf{u}'$ is more significant, at least within the CESM1-LE (Fig. 8). One should be mindful of these limitations when interpreting projections of hydrologic change from PGW simulations.

While our decomposition has clear advantages over that of Seager et al. (2010), it also has drawbacks. For one, it is more computationally demanding, even if it can be performed on a standard desktop computer (see appendix A for ways to improve computational efficiency). It also requires an ensemble that is large enough to accurately represent the temporal distributions of q and T at a given location. In this study, we used 200 simulation years to characterize each climate state (20 ensemble members times 10 years). This turned out to be more than necessary: when we repeated our analysis using only 10 ensemble members, we found nearly identical results (supplemental Fig. 7). Based on the standard definition of climate normals, we speculate that an accurate decomposition

of $\delta \overline{P - E}$ would require at least a few decades of simulation time from each climate, although this will depend on the relative strength of internal variability on decadal and longer time scales.

Despite these challenges, we believe our method opens up promising new avenues to study future changes in the hydrologic cycle. For example, one could use a similar decomposition to investigate the causes of changes in extreme droughts and floods, or extreme vapor transport associated with atmospheric rivers. It would also be interesting to repeat this analysis for different large ensembles of GCM simulations, which are now widely available (e.g., Deser et al. 2020). This might help identify the reasons for differences in model projections of $\delta \overline{P - E}$, and highlight the aspects of $\delta \overline{P - E}$ that are consistent across models, and thus presumably more certain.

Acknowledgments. N. S. was supported by NSF Grant AGS-1954663. D. B. B was supported by the NSF Graduate Research Fellowship Program (NSF Grant DGE1745301). A. D. was supported by NSF Grant AGS-2019647.

Data availability statement. All output from the CESM1 Large Ensemble is publicly available at <https://www.cesm.ucar.edu/community-projects/lens/data-sets>. Analysis codes and post-processed output will be shared upon request.

APPENDIX A

Computing $\overline{P - E}$ from 6-Hourly Model Output

Equation (5) and other equations involving the divergence of vapor transport were computed as follows. First, instantaneous values of q and \mathbf{u} were downloaded at 6-h intervals and regrided from the native hybrid sigma-pressure vertical coordinate system to 29 pressure levels spanning 1000 to 5 hPa. Next, the vertical integral of $q\mathbf{u}$ (or a perturbation thereof) was evaluated at every horizontal grid point. The integrated vapor transport \mathbf{F} at each location was then averaged over the full decade (either 1991–2000 or 2071–80) and all 20 ensemble members. Finally, $\nabla \cdot \mathbf{F}$ was computed using spherical harmonics, and the result was smoothed using a 2D Gaussian filter with $\sigma = 1.25^\circ$, which is close to the grid spacing of the CESM1-LE output (288 longitude points \times 192 latitude points). This filter width has a minimal effect on the spatial pattern of $\overline{P - E}$ while largely eliminating grid-scale noise.

While the vertical integral of $q\mathbf{u}$ is easy to evaluate in principle, looping through each grid point and time step would be prohibitively slow. To speed this up, we first compute the integral numerically using trapezoidal integration on standard pressure levels, and setting $q\mathbf{u} = 0$ at all pressure levels below the surface. This allows the integral to be evaluated at every grid point with a single operation. The problem with this approach is that the range of integration does not extend to the surface, but rather to the first standard pressure level *above* the surface.

The way we correct for this error is illustrated schematically in Fig. A1. The blue shaded area of Fig. A1 represents

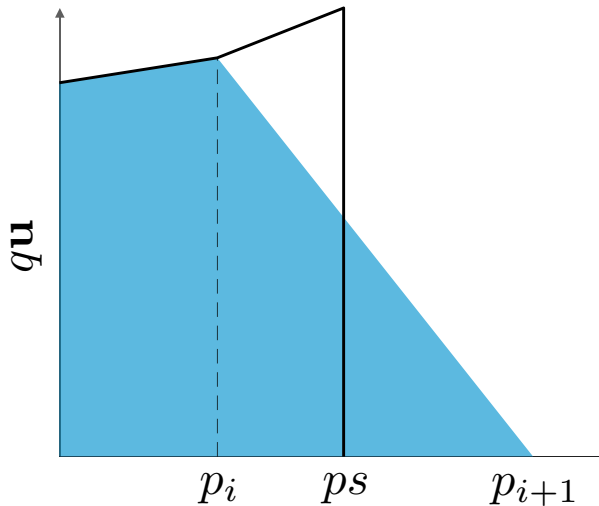


FIG. A1. A schematic illustration of the correction applied to the vertical integral of $q\mathbf{u}$ that is computed using trapezoidal integration on standard pressure levels. The true vertical integral of $q\mathbf{u}$ has a range of integration from $p = 0$ to $p = p_s$ [i.e., from the top of the atmosphere to the surface; Eq. (3)]. An approximation of this integral using trapezoidal integration is represented by the area under the heavy black line, with p_i representing the standard pressure level just above the surface and p_{i+1} representing the standard pressure level just below the surface. The blue shading represents a cruder approximation of the integral on standard pressure levels, with $q\mathbf{u}$ set to 0 at all pressure levels below the surface. The more accurate approximation can be recovered from the crude approximation by subtracting the area of the blue triangle between p_i and p_{i+1} , and adding the area of the trapezoid between p_i and p_s .

the trapezoidal integral of $q\mathbf{u}$ on standard pressure levels, with p_i representing the pressure level just above the surface, and p_{i+1} representing the pressure level just below the surface, where we have set $q\mathbf{u} = 0$. (Note that pressure increases and height decreases to the right in the figure.) A better approximation of the integral would use surface pressure p_s as the upper range of integration, yielding the area under the black contour in Fig. A1. This improved result can be recovered from the original result by subtracting the area of the blue triangle between p_i and p_{i+1} and adding the area of the trapezoid between p_i and p_s . These areas can be computed globally with only a few operations, resulting in much better performance than if nested loops were used to compute the integral independently at each grid point.

Performance was also a consideration in how we chose to compute δq , as depicted in Fig. 2. First, at every location, we removed the means of the q distributions in both the historical and warmer climates to get q' and q'_w . We then sorted q' and q'_w from lowest to highest, and calculated $\delta q'$ as the difference at each percentile of the sorted distributions. Finally, we fit $\delta q'$ to a seventh-order polynomial in q' , and saved the coefficients in a separate file along with the means of each distribution. This allowed δq to be retrieved quickly from q at each grid point and time step.

APPENDIX B

Decomposing $\delta\overline{P-E}_T$ [Eq. (28)]

From Eqs. (20) and (24), $\delta\overline{P-E}_T$ can be written as

$$-\frac{g}{L_v}(\delta\overline{P-E}_T) \approx \nabla \cdot \left[\int_0^{p_s} \overline{\beta\delta\overline{T}q\mathbf{u}} dp + \int_0^{p_s} \overline{\alpha\delta T'(1 + \beta\delta\overline{T})q\mathbf{u}} dp \right], \quad (\text{B1})$$

where both sides have been multiplied by $-g/L_v$ for simplicity. The first term on the RHS of Eq. (B1) represents the contribution from $\delta\overline{T}$, while the second term represents the contribution from $\delta T'$. Applying the product rule to the first term yields

$$\nabla \cdot \int_0^{p_s} \overline{\beta\delta\overline{T}q\mathbf{u}} dp = \int_0^{p_s} \overline{\beta\delta\overline{T}\nabla \cdot (q\mathbf{u})} dp + \int_0^{p_s} \overline{\nabla(\beta\delta\overline{T}) \cdot (q\mathbf{u})} dp + \beta_s \overline{\delta\overline{T}_s (q_s \mathbf{u}_s \nabla p_s)}. \quad (\text{B2})$$

From Eq. (27), the first term on the RHS of Eq. (B2) can be further decomposed as

$$\int_0^{p_s} \overline{\beta\delta\overline{T}\nabla \cdot (q\mathbf{u})} dp = \beta_s \overline{\delta\overline{T}_s} \int_0^{p_s} \overline{\nabla \cdot (q\mathbf{u})} dp + \int_0^{p_s} \overline{(\beta\delta\overline{T} - \beta_s \delta\overline{T}_s) \nabla \cdot (q\mathbf{u})} dp. \quad (\text{B3})$$

Finally, the first term on the RHS of Eq. (B3) and the last term on the RHS of Eq. (B2) combine to give

$$\beta_s \overline{\delta\overline{T}_s} \left[\int_0^{p_s} \overline{\nabla \cdot (q\mathbf{u})} dp + \overline{q_s \mathbf{u}_s \nabla p_s} \right] = \beta_s \overline{\delta\overline{T}_s} \nabla \cdot \int_0^{p_s} \overline{q\mathbf{u}} dp = -\frac{g}{L_v} \beta_s \overline{\delta\overline{T}_s} (\overline{P-E}), \quad (\text{B4})$$

where the final equality follows from Eq. (3). Combining Eqs. (B1)–(B4) yields Eq. (28).

REFERENCES

- Bengtsson, L., K. I. Hodges, and N. Keenlyside, 2009: Will extratropical storms intensify in a warmer climate? *J. Climate*, **22**, 2276–2301, <https://doi.org/10.1175/2008JCLI2678.1>.
- Bonan, D. B., N. Siler, G. H. Roe, and K. C. Armour, 2023: Energetic constraints on the pattern of changes to the hydrological cycle under global warming. *J. Climate*, **36**, 3499–3522, <https://doi.org/10.1175/JCLI-D-22-0337.1>.
- Boos, W. R., 2012: Thermodynamic scaling of the hydrological cycle of the last glacial maximum. *J. Climate*, **25**, 992–1006, <https://doi.org/10.1175/JCLI-D-11-00010.1>.
- Byrne, M. P., and P. A. O’Gorman, 2015: The response of precipitation minus evapotranspiration to climate warming: Why the “wet-get-wetter, dry-get-drier” scaling does not hold over land. *J. Climate*, **28**, 8078–8092, <https://doi.org/10.1175/JCLI-D-15-0369.1>.
- , and T. Schneider, 2016: Narrowing of the ITCZ in a warming climate: Physical mechanisms. *Geophys. Res. Lett.*, **43**, 11 350–11 357, <https://doi.org/10.1002/2016GL070396>.

- , and P. A. O’Gorman, 2018: Trends in continental temperature and humidity directly linked to ocean warming. *Proc. Natl. Acad. Sci. USA*, **115**, 4863–4868, <https://doi.org/10.1073/pnas.1722312115>.
- , A. G. Pendergrass, A. D. Rapp, and K. R. Wodzicki, 2018: Response of the intertropical convergence zone to climate change: Location, width, and strength. *Curr. Climate Change Rep.*, **4**, 355–370, <https://doi.org/10.1007/s40641-018-0110-5>.
- Chou, C., and J. D. Neelin, 2004: Mechanisms of global warming impacts on regional tropical precipitation. *J. Climate*, **17**, 2688–2701, [https://doi.org/10.1175/1520-0442\(2004\)017<2688:MOGWIO>2.0.CO;2](https://doi.org/10.1175/1520-0442(2004)017<2688:MOGWIO>2.0.CO;2).
- de Boyer Montégut, C., J. Mignot, A. Lazar, and S. Cravatte, 2007: Control of salinity on the mixed layer depth in the world ocean: 1. General description. *J. Geophys. Res.*, **112**, C06011, <https://doi.org/10.1029/2006JC003953>.
- Deser, C., A. Phillips, V. Bourdette, and H. Teng, 2012: Uncertainty in climate change projections: The role of internal variability. *Climate Dyn.*, **38**, 527–546, <https://doi.org/10.1007/s00382-010-0977-x>.
- , and Coauthors, 2020: Insights from Earth system model initial-condition large ensembles and future prospects. *Nat. Climate Change*, **10**, 277–286, <https://doi.org/10.1038/s41558-020-0731-2>.
- DiNezio, P. N., G. A. Vecchi, and A. C. Clement, 2013: Detectability of changes in the Walker circulation in response to global warming. *J. Climate*, **26**, 4038–4048, <https://doi.org/10.1175/JCLI-D-12-00531.1>.
- Donohoe, A., A. R. Atwood, and M. P. Byrne, 2019: Controls on the width of tropical precipitation and its contraction under global warming. *Geophys. Res. Lett.*, **46**, 9958–9967, <https://doi.org/10.1029/2019GL082969>.
- Feldl, N., S. Po-Chedley, H. K. A. Singh, S. Hay, and P. J. Kushner, 2020: Sea ice and atmospheric circulation shape the high-latitude lapse rate feedback. *npj Climate Atmos. Sci.*, **3**, 41, <https://doi.org/10.1038/s41612-020-00146-7>.
- Held, I. M., and B. J. Soden, 2006: Robust responses of the hydrological cycle to global warming. *J. Climate*, **19**, 5686–5699, <https://doi.org/10.1175/JCLI3990.1>.
- Kang, S. M., and J. Lu, 2012: Expansion of the Hadley cell under global warming: Winter versus summer. *J. Climate*, **25**, 8387–8393, <https://doi.org/10.1175/JCLI-D-12-00323.1>.
- Kay, J. E., and Coauthors, 2015: The Community Earth System Model (CESM) large ensemble project: A community resource for studying climate change in the presence of internal climate variability. *Bull. Amer. Meteor. Soc.*, **96**, 1333–1349, <https://doi.org/10.1175/BAMS-D-13-00255.1>.
- Liu, M., G. Vecchi, B. Soden, W. Yang, and B. Zhang, 2021: Enhanced hydrological cycle increases ocean heat uptake and moderates transient climate change. *Nat. Climate Change*, **11**, 848–853, <https://doi.org/10.1038/s41558-021-01152-0>.
- Lu, J., G. A. Vecchi, and T. Reichler, 2007: Expansion of the Hadley cell under global warming. *Geophys. Res. Lett.*, **34**, L06805, <https://doi.org/10.1029/2006GL028443>.
- Marshall, J., J. R. Scott, K. C. Armour, J.-M. Campin, M. Kelley, and A. Romanou, 2015: The ocean’s role in the transient response of climate to abrupt greenhouse gas forcing. *Climate Dyn.*, **44**, 2287–2299, <https://doi.org/10.1007/s00382-014-2308-0>.
- Menary, M. B., and R. A. Wood, 2018: An anatomy of the projected North Atlantic warming hole in CMIP5 models. *Climate Dyn.*, **50**, 3063–3080, <https://doi.org/10.1007/s00382-017-3793-8>.
- Norris, J., G. Chen, and J. D. Neelin, 2019: Thermodynamic versus dynamic controls on extreme precipitation in a warming climate from the Community Earth System Model large ensemble. *J. Climate*, **32**, 1025–1045, <https://doi.org/10.1175/JCLI-D-18-0302.1>.
- O’Gorman, P. A., 2010: Understanding the varied response of the extratropical storm tracks to climate change. *Proc. Natl. Acad. Sci. USA*, **107**, 19176–19180, <https://doi.org/10.1073/pnas.1011547107>.
- , 2015: Precipitation extremes under climate change. *Curr. Climate Change Rep.*, **1**, 49–59, <https://doi.org/10.1007/s40641-015-0009-3>.
- , and T. Schneider, 2008: Energy of midlatitude transient eddies in idealized simulations of changed climates. *J. Climate*, **21**, 5797–5806, <https://doi.org/10.1175/2008JCLI2099.1>.
- Oki, T., and S. Kanae, 2006: Global hydrological cycles and world water resources. *Science*, **313**, 1068–1072, <https://doi.org/10.1126/SCIENCE.1128845>.
- Pfahl, S., P. A. O’Gorman, and E. M. Fischer, 2017: Understanding the regional pattern of projected future changes in extreme precipitation. *Nat. Climate Change*, **7**, 423–427, <https://doi.org/10.1038/nclimate3287>.
- Power, S. B., and G. Kociuba, 2011: The impact of global warming on the Southern Oscillation Index. *Climate Dyn.*, **37**, 1745–1754, <https://doi.org/10.1007/s00382-010-0951-7>.
- Scheff, J., and D. Frierson, 2012: Twenty-first-century multimodel subtropical precipitation declines are mostly midlatitude shifts. *J. Climate*, **25**, 4330–4347, <https://doi.org/10.1175/JCLI-D-11-00393.1>.
- Screen, J. A., 2014: Arctic amplification decreases temperature variance in northern mid- to high-latitudes. *Nat. Climate Change*, **4**, 577–582, <https://doi.org/10.1038/nclimate2268>.
- Seager, R., N. Naik, and G. A. Vecchi, 2010: Thermodynamic and dynamic mechanisms for large-scale changes in the hydrological cycle in response to global warming. *J. Climate*, **23**, 4651–4668, <https://doi.org/10.1175/2010JCLI3655.1>.
- Siler, N., G. H. Roe, and K. C. Armour, 2018: Insights into the zonal-mean response of the hydrologic cycle to global warming from a diffusive energy balance model. *J. Climate*, **31**, 7481–7493, <https://doi.org/10.1175/JCLI-D-18-0081.1>.
- Smith, S., P. W. Staten, and J. Lu, 2021: How moist and dry intrusions control the local hydrologic cycle in present and future climates. *J. Climate*, **34**, 4343–4359, <https://doi.org/10.1175/JCLI-D-20-0780.1>.
- Taylor, P. C., and Coauthors, 2022: Process drivers, inter-model spread, and the path forward: A review of amplified Arctic warming. *Front. Earth Sci.*, **9**, 758361, <https://doi.org/10.3389/feart.2021.758361>.
- Trenberth, K. E., and C. J. Guillemot, 1995: Evaluation of the global atmospheric moisture budget as seen from analyses. *J. Climate*, **8**, 2255–2272, [https://doi.org/10.1175/1520-0442\(1995\)008<2255:EOTGAM>2.0.CO;2](https://doi.org/10.1175/1520-0442(1995)008<2255:EOTGAM>2.0.CO;2).
- Wetherald, R. T., and S. Manabe, 2002: Simulation of hydrologic changes associated with global warming. *J. Geophys. Res.*, **107**, 4379, <https://doi.org/10.1029/2001JD001195>.
- Wills, R. C., M. P. Byrne, and T. Schneider, 2016: Thermodynamic and dynamic controls on changes in the zonally anomalous hydrological cycle. *Geophys. Res. Lett.*, **43**, 4640–4649, <https://doi.org/10.1002/2016GL068418>.
- Wu, Y., M. Ting, R. Seager, H.-P. Huang, and M. A. Cane, 2011: Changes in storm tracks and energy transports in a warmer climate simulated by the GFDL CM2.1 model. *Climate Dyn.*, **37**, 53–72, <https://doi.org/10.1007/s00382-010-0776-4>.